Static and dynamic calibration of torsional spring constants of cantilevers

Aleksander Labuda,[1] Changhong Cao,[2] Tim Walsh,[1] Jieh Meinhold,[1] Roger Proksch,[1] Yu Sun,[2] and Tobin Filleter[2]

[1]*Asylum Research an Oxford Instruments Company, Santa Barbara, California 93117, USA*
[2]*Department of Mechanical and Industrial Engineering, University of Toronto, Toronto, Ontario M5S 3G8, Canada*

A method for calibrating the dynamic torsional spring constant of cantilevers by directly measuring the thermally driven motion of the cantilever with an interferometer is presented. Random errors in calibration were made negligible (<1%) by averaging over multiple measurements. The errors in accuracy of ±5% or ±10% for both of the cantilevers calibrated in this study were limited only by the accuracy of the laser Doppler vibrometer (LDV) used to measure thermal fluctuations. This is a significant improvement over commonly used methods that result in large and untraceable errors resulting from assumptions made about the cantilever geometry, material properties, and/or hydrodynamic physics of the surroundings. Subsequently, the static torsional spring constant is determined from its dynamic counterpart after careful LDV measurements of the torsional mode shape, backed by finite element analysis simulations. A meticulously calibrated cantilever is used in a friction force microscopy experiment that measures the friction difference and interfacial shear strength (ISS) between graphene and a silicon dioxide AFM probe. Accurate calibration can resolve discrepancies between different experimental methods, which have contributed to a large scatter in the reported friction and ISS values in the literature to date. *Published by AIP Publishing.* https://doi.org/10.1063/1.5045679

I. INTRODUCTION

Atomic force microscopy enables unique tribological experiments to be performed because a single asperity nanoscale contact can be studied. More specifically, friction force microscopy is used to study the fundamental phenomena that define friction at the nanoscale by measuring the lateral forces between the tip and a sample. Quantifying lateral forces occurring at the tip-sample contact is necessary in accurately studying friction phenomena and allows for a direct comparison of lateral forces between experiments,[1–5] simulations,[6–9] and theory.[10–13]

The desire for quantitative measurements of lateral forces has led to extensive research in cantilever calibration itself.[14–26] Most of these methods involve modeling of the cantilever and/or its hydrodynamic surroundings[27] or require destructive experimental procedures that may damage the tip apex.[28]

This paper presents methodology for calibrating the dynamic torsional spring constant of a cantilever directly using an interferometric sensor. The only assumption is that the equipartition theorem holds true: the average energy of the torsional mode is $\frac{1}{2}k_BT$. The simplicity of the method allows straightforward error analysis that can be used to track calibration errors. Finally, static torsional stiffness is calculated from the dynamic stiffness through an analysis of static and dynamic mode shapes.

II. TORSIONAL CALIBRATION METHODS

A. Instrument

An Asylum Research Cypher AFM was interfaced with a Polytec laser Doppler vibrometer (LDV) through a modified blueDrive™[29] optical beam positioning unit. This combined system focuses the LDV laser to a 3-μm spot size and programmatically positions the laser spot anywhere on the cantilever with 100-nm precision. Because the measurement is interferometric in nature, the sensitivity (nm/V) is based on the wavelength of light and accurately predetermined in-factory.

This instrument enables quantitative *in situ* mapping of driven cantilever dynamics, as used elsewhere,[30] as well as the calibration of cantilever spring constants through measurement of thermal noise spectra.[31,32] The cantilevers characterized in this experiment are the Nanosensors™ PPP-CONTR and PPP-FM.

B. Spectrogram calibration method

The measured amplitude of the cantilever thermal motion depends on the location and the eigenmode (resonance mode) in question. The power spectral density (PSD) conveniently separates the contributions from different eigenmodes at any particular cantilever location, as shown in Fig. 1(a) for a laser spot positioned at the far edge of the cantilever.

By scanning the laser spot across the cantilever widthwise and acquiring successive PSDs, a spectrogram of the thermal motion can be constructed, as in Fig. 1(b). Out of the four observed eigenmodes, one is clearly the first torsional mode of the cantilever because its motion reaches zero at the cantilever center.

Fitting the identified torsional spectrum of each successive PSD with a simple harmonic oscillator (SHO) model provides a measure of the amplitude variance A_{rms}^2 at every position. These amplitude fluctuations can be calculated across the cantilever by integrating each SHO fit, as shown in Fig. 1(c).
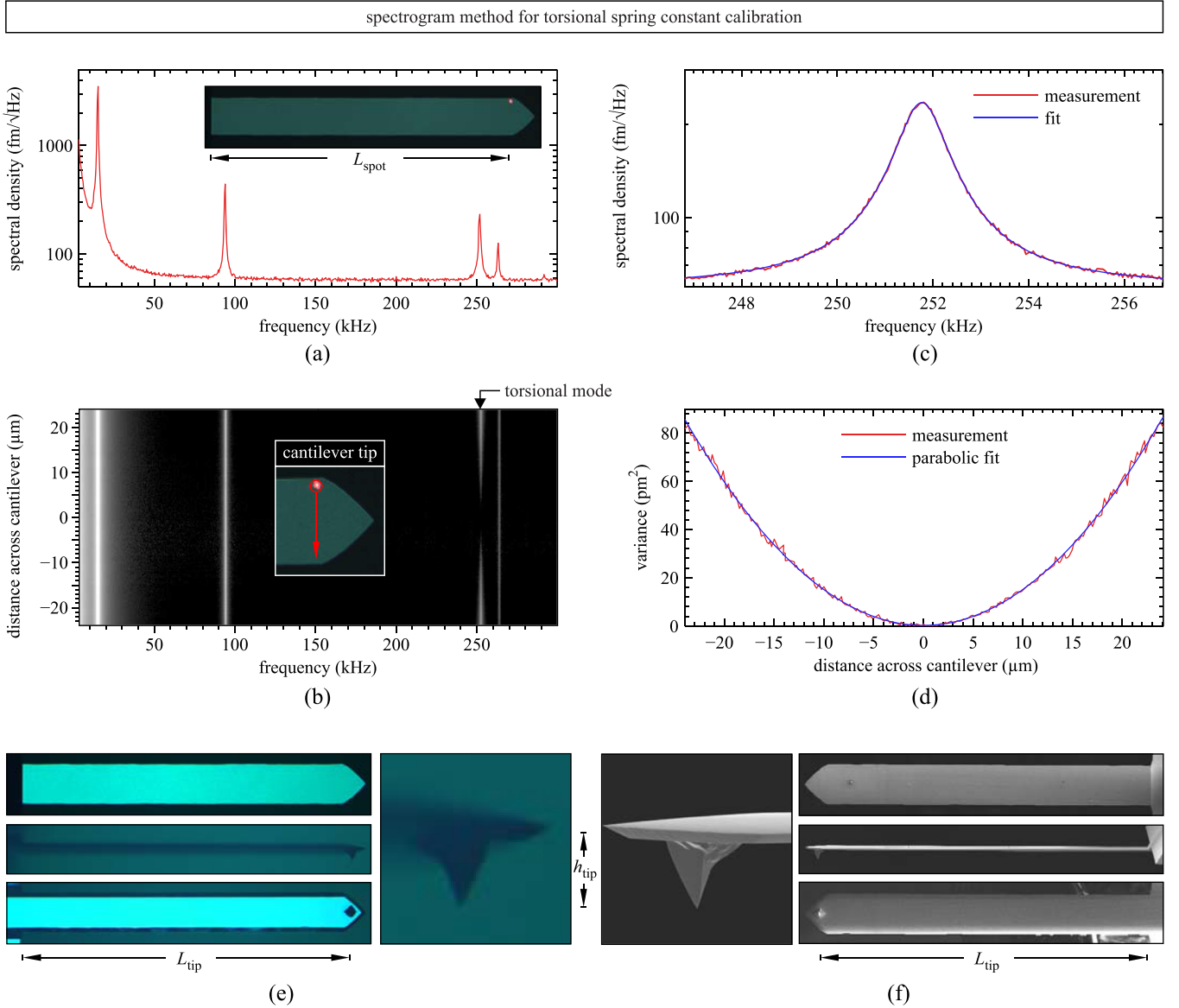
spectrogram method for torsional spring constant calibration

(a)

(c)

(b)

(d)

(e)

(f)

FIG. 1. The spectrogram method performed on a PPP-CONTR cantilever at a distance L_{spot} from the cantilever base. (a) The PSD of the cantilever thermal motion (computed by the Daniell method[33]) was measured at various distances across the cantilever to create (b) a spectrogram where the spectral density is represented in a gray scale. (c) The torsional peak can be identified and fit with a SHO model to determine the amplitude variance A_{rms}^2 as a function of distance across the cantilever. (d) Fitting the data with Eq. (3) returns the torsional spring constant $k_{\theta_{AC}}$. Obtaining the lateral spring constant k_L requires the tip height h_{tip} taken from either (e) optical photographs by the Cypher AFM or (f) scanning electron microscope images. Ten spectrogram calibrations of this cantilever resulted in $k_{\theta_{AC}} = 26.8 \pm 0.2$ nN m and $k_{L_{AC}} = 121 \pm 4$ N/m. Table III in the Appendix summarizes the parameters used for calculating these spring constants.

For a cantilever that does not bend along its width and only rotates laterally due to torsional motion, the measured amplitude A is related to the torsional angle of the cantilever θ by the radial distance $d_\perp$, as in

$$A = d_\perp \theta. \tag{1}$$

By the equipartition theorem, the torsional fluctuations obey

$$\frac{1}{2} k_{\theta_{AC}} \theta_{rms}^2 = \frac{1}{2} k_B T, \tag{2}$$

where the dynamic torsional spring constant $k_{\theta_{AC}}$ is related to the Boltzmann constant k_B and the temperature T. Combining both equations predicts that

$$A_{rms}^2 = \frac{k_B T}{k_{\theta_{AC}}} d_\perp^2. \tag{3}$$

Conveniently, this parabolic relationship can be fit to the data in Fig. 1(d), resulting in a measurement of $k_{\theta_{AC}}$. The accuracy of the fit suggests that the model presented so far is appropriate and that the LDV measurement is linear.

Note that the torsional fluctuations were not measured exactly at the tip location, as can be understood by inspection of Fig. 1, where $L_{spot} \neq L_{tip}$. A small correction factor for this discrepancy (-0.7%) was applied from knowledge of the torsional mode shape (determined in Sec. III).

The spectrogram calibration method is an elegant way of measuring $k_{\theta_{AC}}$ and is worthwhile performing at least once to validate the assumptions leading up to Eq. (3) to verify the stability of the system and the linearity of the LDV. However, this method is not efficient because most of the time is spent measuring no signal near the center of the

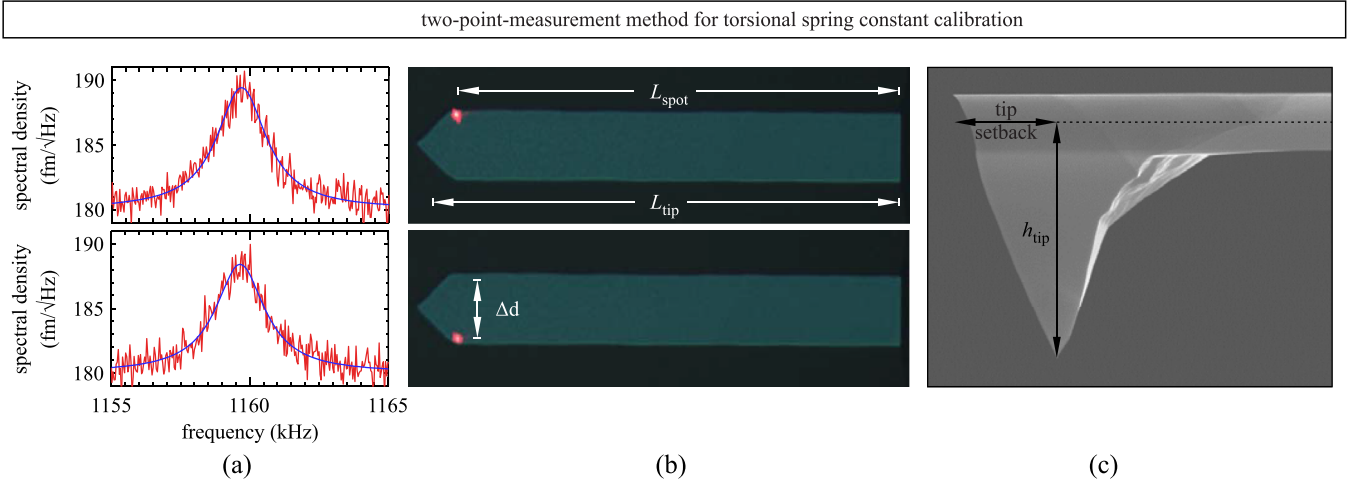| two-point-measurement method for torsional spring constant calibration |
|---|

FIG. 2. The two-point calibration method was performed on a PPP-FM cantilever. (a) The thermal noise was measured at two locations; (b) the distance between both laser spot locations was determined optically; and the distance of the laser spot to the base was also determined optically, while the distance to the tip used (c) an SEM image of the cantilever. The torsional spring constant was calculated by Eq. (5) as $k_{\theta_{AC}} = 66.4 \pm 0.5$ nN m from ten repeated measurements. The lateral spring constant $k_{L_{AC}} = 284 \pm 5$ N/m from a tip height SEM measurement. Table III in the Appendix summarizes the parameters used for calculating these spring constants.

cantilever. Section II C presents a more time-efficient method for measuring $k_{\theta_{AC}}$.

C. Two-point calibration method

The torsional calibration can be sped up by measuring the amplitude variance A_{rms}^2 only near the edges of the cantilever, where the signal-to-noise ratio is highest. In fact, because the parabolic function [Eq. (3)] fits the data impeccably in Fig. 1(d), only two measurements are required to define k_θ accurately.

Two amplitude measurements (A_1, A_2) at any two positions across the cantilever allow the determination of the cantilever angle by

$$\theta = \frac{A_1 - A_2}{\Delta d_\perp},\qquad(4)$$

where only the distance between both positions $\Delta d_\perp$ is required. This conveniently avoids the need to define the cantilever center and reduces any associated errors. Note that the amplitudes, as defined here, differ in sign if measured on either side of the cantilever long-axis.

Here, the torsional spring constant is measured directly by

$$k_{\theta_{AC}} = \frac{k_B T}{(A_{\text{rms},1} + A_{\text{rms},2})^2}\Delta d_\perp^2.\qquad(5)$$

This method was performed on a cantilever in Fig. 2.

The stiffness correction for the misalignment between the laser spot and the cantilever tip ($L_{\text{spot}} \neq L_{\text{tip}}$ as seen in Fig. 2) was −0.2% as calculated from the torsional mode shape (determined in Sec. III).

III. DYNAMIC TO STATIC CONVERSION

So far, the dynamic stiffness of the first eigenmode was measured by virtue of using the thermal noise as a signal. This section relates the dynamic torsional stiffness $k_{\theta_{AC}}$ to the static torsional stiffness $k_{\theta_{DC}}$. The mode shapes of both

static and dynamic torsional modes (ϕ_{DC} and ϕ_{AC}) relate both stiffnesses by[50]

$$\frac{k_{\theta_{AC}}}{k_{\theta_{DC}}} = \frac{\int_0^1 \left(\frac{\partial\phi_{AC}(x)}{\partial x}\right)^2 dx}{\int_0^1 \left(\frac{\partial\phi_{DC}(x)}{\partial x}\right)^2 dx},\qquad(6)$$

where x is the distance along the long axis of the cantilever, normalized such that $x = 1$ is at the cantilever end.

Note that this treatment is analogous to normal deflection modes,[34,35] where the static stiffness is ~3% softer than the first eigenmode stiffness for an ideal Euler-Bernoulli beam because of slight differences in the mode shape.[36] This distinction is often disregarded due to the small discrepancy. However, in the context of torsional modes, the static and the first dynamic mode shapes differ substantially.

For an ideal circular shaft fixed at one end, the first eigenmode shape analytically solves to[36]

$$\phi_{AC}(x) = \sin\left(\frac{\pi}{2}x\right),\qquad(7)$$

while the static mode shape is simply linear, as in

$$\phi_{DC}(x) = x.\qquad(8)$$

In this case, Eq. (6) becomes

$$\frac{k_{\phi_{AC}}}{k_{\phi_{DC}}} = \frac{\pi^2}{8} \approx 1.234.\qquad(9)$$

For the record, higher eigenmode shapes correspond to odd harmonics of the first sinusoidal eigenmode shape in Eq. (7), but they are not studied here.

The assumption of circular symmetry [necessary to derive Eq. (9)] is not met in practice. Real cantilevers typically have a rectangular or trapezoidal cross section with a large aspect ratio. Non-axisymmetric beams undergo warping when torsion

is applied.[36] This changes the mode shape slightly near the cantilever base, as observed by the LDV mode shape mapping in Fig. 3(a). Finite element analysis (FEA) of a cantilever with identical dimensions reproduces the measured mode shape very closely. The deviation from expected behavior near the cantilever base is caused by in-plane compression/tension waves that dominate over the transverse shear waves that make up the mode shape [as confirmed by inspection of FEA results and depicted in Fig. 3(a)].

Furthermore, real cantilevers have tip masses and tapered plan views, such as the PPP-CONTR and PPP-FM cantilevers measured so far. FEA simulations, backed by LDV measurements, demonstrate only modest mode shape differences relative to an ideal circular shaft, as shown in Fig. 3(b). In this case, the additional amount of the mode shape curvature contributed to an increase in $k_{\theta_{AC}}$ relative to circular shaft theory; however, the increase was well within the 10% measurement error of the LDV.

Given the modest deviations between these real cantilever and ideal circular shafts, Eq. (9) can be used as a good approximation for relating $k_{\theta_{AC}}$ to $k_{\theta_{DC}}$ for the cantilevers characterized so far. This is expected to be a conservative estimate
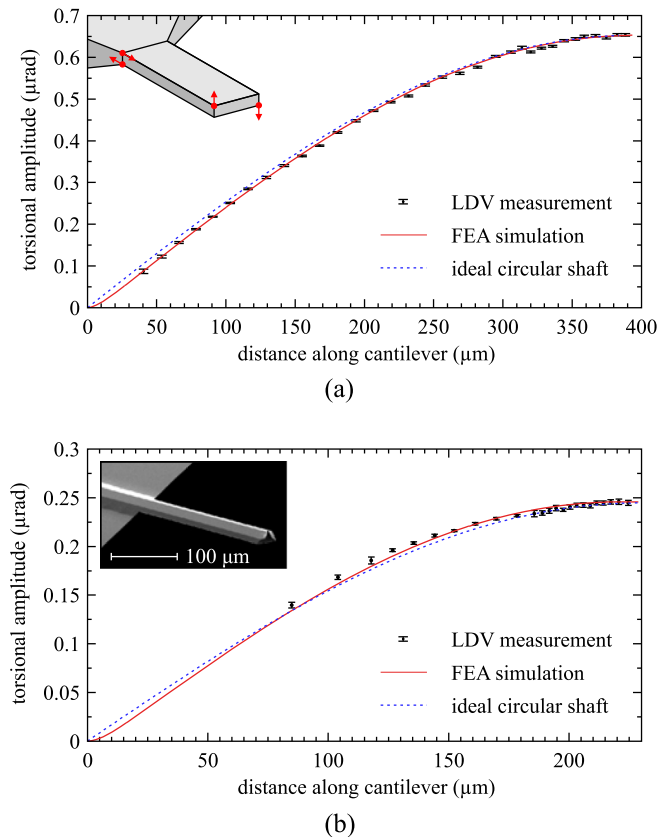

(a)

(b)

FIG. 3. (a) A cantilever that is the closest available representation of an Euler-Bernoulli beam (NOCAL) was driven at its first torsional resonance frequency. The LDV measurement of the torsional mode shape matches the FEA simulation very closely (no fitting parameters were used other than scaling the amplitude of the FEA result). Due to the rectangular cross section, the mode shape deviates from an ideal circular shaft. This deviation is caused by an in-plane compression/tension profile, which is depicted by arrows on the inset cantilever. (b) The mode shape of the PPP-FM cantilever used in Fig. 2 was measured, and FEA was performed. The tip mass causes some additional deviations from circular shaft theory that increases the torsional stiffness.

as non-idealities cause an additional curvature in the torsional mode shape, and Eq. (9) does not account for in-plane compression/tension that also stores energy during oscillation.

More rigorous FEA studies are necessary to obtain accurate estimate of $k_{\theta_{AC}}/k_{\theta_{DC}}$ for intricate cantilever geometries. In the interim, the relationship from Eq. (9) was used to analyze the data presented in this paper.

IV. TORSIONAL TO LATERAL CONVERSION

In previous sections, the torsional spring constant was measured. The lateral spring constant requires the tip height h_{tip} and can be calculated by

$$k_L = \frac{k_\theta}{h_{\text{tip}}^2},$$ (10)

where k_θ may represent the static or dynamic stiffness depending on the context. The tip height was measured by an optical photograph, as well as by SEM imaging, as shown in Fig. 1.

With a known cantilever lateral stiffness, the sensitivity of the optical beam deflection system (in units of nm/V) can be calibrated by measuring the thermal motion of the cantilever and enforcing the equipartition theorem. This is typically performed for normal deflection of the cantilever[37,38] but applies to the lateral deflection as well. However, there are complications that arise for typical cantilevers when calibrating the lateral sensitivity: the lateral stiffness of the tip apex[17] and the in-plane lateral bending stiffness[16] of the cantilever may be comparable in magnitude to the lateral stiffness of the cantilever measured so far. The consequence of having these three springs in series is that the true displacement of the tip may be significantly underestimated:[39] some of the displacement is caused by the tip apex and in-plane bending which are *not* measured by the optical beam deflection system which is only sensitive to angular changes in the cantilever. Quantitative interpretation of the lateral displacement of the tip apex in a friction force microscopy experiment requires careful consideration of these sources of error.

Other considerations, such as the coupling of normal and lateral forces due to the cantilever tilt,[40] should also be considered when interpreting tip-sample interactions.

V. ERROR ANALYSIS

The fact that the calibration procedures presented so far take direct measurements of torsional thermal fluctuations allows for a meaningful error analysis, as presented in this section. By Eq. (3), errors in k_θ arise from errors in A_{rms}^2 and $\Delta d_\perp^2$, both of which will now be discussed in terms of accuracy and precision.

The Cypher AFM optics were calibrated with a calibration grid and determined to be 99.5% accurate across the field of view, leading to relative errors <1% on $\Delta d_\perp^2$. These sources of error are negligible compared to errors in A_{rms}^2 due to the limited accuracy[51] of the LDV and frequency dependence of its signal response. For the PPP-CONTR cantilever, there is an estimated error of roughly ±5% in A_{rms}^2, which translates directly to errors in k_θ. For the PPP-FM cantilever, this error

is estimated at ±10% because the error is larger at a high frequency for this LDV. Note that these errors are specific to the particular LDV model used here and not inherent to the LDV method itself, which may be much more accurate on different interferometric sensors.

On the other hand, all sources of random errors in the calibration were measured by repeating the calibration procedure ten times for each cantilever. This was deemed sufficient as the random errors (<1%) fell well below the accuracy errors described in the previous paragraph. These repeated measurements account for random errors in both A_{rms}^2 and $\Delta d_\perp^2$ simultaneously.

Finally, calibrating the lateral spring constant k_L introduces errors associated mostly with measuring the tip height. In this case, SEM images lead to a significant reduction in the error with respect to optical images. In fact, the error in the SEM-measured tip height is overshadowed by the errors in accuracy in measuring k_θ in the first place.

VI. COMPARISON OF CALIBRATION METHODS

Both calibration methods presented so far (collectively referred to as the LDV method henceforth) are now compared to two commonly used calibration methods: the geometry method[41] and the Sader method.[27] The mathematics behind these methods are presented in the Appendix, while the results are presented in Table I.

The geometry and Sader methods for measuring $k_{\theta_{DC}}$ both assume that the cantilever has a rectangular cross section with a length that greatly exceeds the width, a width that greatly exceeds the thickness, and the absence of a cantilever tip. Furthermore, the geometry method requires knowledge of the elastic and shear moduli, which can vary significantly.[42,43] Also, the Sader method assumes planar laminar flow around the cantilever by an incompressible fluid[44] and assumes that the tip is at the very end of the cantilever. Because of these limitations, an accurate error analysis is difficult for these two calibration methods, and only the calibration of cantilevers with specific geometries is possible.

TABLE I. Comparison of methods for the torsional and lateral spring constant calibrations for the PPP-CONTR and PPP-FM cantilevers. The reported errors are random errors that stem from averaging ten repeated measurements. The accuracy of the PPP-CONTR calibration is ±5%. The accuracy of the PPP-FM calibration is ±10%. Table I in the Appendix summarizes the parameters used for calculating these spring constants.

		Static torsional spring constant $k_{\theta_{DC}}$ (10^{-9} N m/rad)	Static lateral spring constant $k_{L_{DC}}$ (N/m)
PPP-CONTR	Geometry method	26.9	113
	Sader method	20.6	86.8
	LDV method	21.7 ± 0.2	98 ± 3
PPP-FM	Geometry method	86.0	415
	Sader method	57.0	275
	LDV method	53.8 ± 0.5	230 ± 4

The trapezoidal cross section of these cantilevers, the aluminum coating on the PPP-CONTR cantilever, variations in moduli, the existence of a tip, as well as deviations from ideal hydrodynamic behavior may contribute to the deviations between the calibration methods presented in Table I.

On the other hand, the LDV method for measuring $k_{\theta_{AC}}$ only assumes that the torsional mode is solely driven by thermal forces, which is a very good approximation in ambient conditions. This fact enabled the meaningful error analysis performed in Sec. V. Importantly, the lack of assumption allows the LDV method to calibrate cantilevers of the arbitrary shape. Finally, although the mode shape correction factor that relates $k_{\theta_{AC}}$ to $k_{\theta_{DC}}$ was derived for an ideal circular shaft, it can be refined by FEA simulations and backed by LDV mode shape measurements.

An important distinction of the LDV method is that it natively measures the dynamic spring constant, while the static spring constant is inferred from the mode shape. On the other hand, the geometry and Sader methods measure the static spring constant of the cantilever directly. Depending on the context, either $k_{\theta_{AC}}$ or $k_{\theta_{DC}}$ may be required. Experiments with driven torsional modes require the use of $k_{\theta_{AC}}$, while typical sub-resonance friction force microscopy requires the use of $k_{\theta_{DC}}$.

As can be seen in Table I, the Sader method agrees more closely to the measurements taken with the LDV method than to the geometry method for the specific cantilever geometries tested here. The geometry method highly overestimates k_θ presumably because it is based on assumptions that are far from valid in practice. It is, however, difficult to draw strong conclusions about the absolute accuracy of the Sader method versus the geometry method until larger scale studies are performed.

Finally, it is important to note that instruments based on the optical beam defection (OBD) method are in principle better suited than a LDV for calibrating the torsional spring constant of cantilevers. This is because the OBD method measures the angular deflection of the cantilever by nature,[45] which is the native variable for cantilever torsion as can be understood from Eq. (2). Such instruments can also map the mode shape of cantilevers[46,47] as was performed here. However, due to their limited accuracy, these methods do not provide an absolute calibration standard. Although the LDV and other interferometric methods natively measure the displacement of the cantilever, as opposed to its angular deflection, the fact that they are inherently calibrated by the wavelength of light makes them more suited for the high accuracy calibration of cantilever spring constants.

VII. RESULTS

The PPP-FM cantilever calibrated in Fig. 2 was used to measure the lateral force in a friction force microscopy experiment performed on graphene-on-silicon dioxide and pure silicon dioxide substrates as a function of the applied normal load. The experiment is summarized in Fig. 4.

The relationship between the lateral force and normal load was fit to a Maugis–Dugdale model[12] for data on graphene and on silicon dioxide. The resulting fit parameters (pull-off force
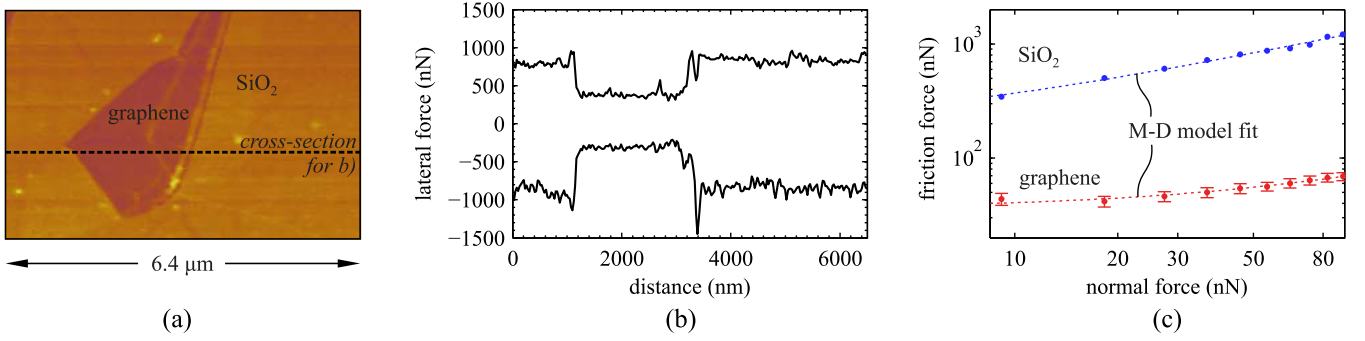
FIG. 4. (a) Lateral force map of graphene on silicon dioxide is shown. (b) Trace and retrace of the lateral force from the cross section in (a) is plotted. (c) The lateral forces on silicon dioxide and graphene were averaged for the whole image in (a) and plotted versus the normal force. The Maugis-Dugdale model (dashed line) was fit to the data. The static lateral stiffness was calibrated in Fig. 2 to $k_{LDC} = 230 \pm 4$ N/m with ±10% error in accuracy. The normal spring constant was measured to be 3.17 ± 0.03 N/m with ±5% accuracy using a protocol established elsewhere.[32]

TABLE II. Summary of the ISS measured in Fig. 4 and a comparison to other experiments.

	Interfacial shear strength (MPa)	
	Tip to graphene	Tip to SiO_2
LDV method	128	1715
Sader method	112	1510
Geometry method	169	2280
Chen and Filleter[48]	173 ± 13	1930 ± 282

and contact radius) can be used to calculate the interfacial shear strength (ISS) between the AFM tip and the contact substrate according to Carpick's fitting protocol.[13]

Whereas the lateral-to-normal relationship on both graphene and SiO_2 is qualitatively consistent with previous experiments,[49] the resulting interfacial shear strengths differ from those measured herein (see Table II). The quantitative discrepancy may be attributed in part to errors in torsional calibration methods. The LDV method for the direct calibration of torsional spring constants can be used as a standard with traceable errors for the reducing scatter in friction and ISS measurement of future experiments.

VIII. CONCLUSION

A method was presented for measuring the dynamic torsional spring constant of a cantilever by direct interferometric measurement of its torsional thermal fluctuations: the LDV method. By avoiding assumptions about the cantilever geometry, material properties, and/or the hydrodynamic properties of its environment, the LDV method allows the calibration of cantilevers of arbitrary shapes with high accuracy.

The static torsional spring constant can be calculated from the dynamic one by mode shape analysis. Analytical approximations of mode shapes were shown to be good approximations and can be refined through FEA simulations or direct mode shape measurement by LDV mapping.

The lateral spring constant can be calculated from the torsional spring constant with knowledge of the tip height: measured either optically or, ideally, from a SEM image of the cantilever.

A cantilever with a calibrated lateral stiffness within ±10% accuracy and <1% random error was used to measure the friction and interfacial shear stress (ISS) between a silicon dioxide AFM tip and graphene. Such quantitative studies may help to explain the quantitative scatter in the measured friction and ISS in experiments to date and allow for a more meaningful comparison to simulations and theory used to improve our understanding of nanoscale phenomena.

APPENDIX: MATHEMATICAL DETAILS

1. Geometry method

The geometry method assumes that the cantilever can be described as an Euler-Bernoulli beam and directly calculates the torsional stiffness from the shear modulus G, the width w, the thickness t, and the length L of the beam by[41]

$$k_{\theta_{DC}} = \frac{Gwt^3}{3L}. \qquad (A1)$$

In the absence of a high quality side-view SEM image of the cantilever, an indirect measurement of thickness t^* may be inferred from a measurement of the first normal resonance frequency f_N by[41]

$$t^* = \frac{2\sqrt{12}\pi}{1.875^2}\sqrt{\frac{\rho_c}{E}} \times f_N \times L^2, \qquad (A2)$$

where ρ_c is the density of the cantilever material and E is Young's modulus. This equation applies to singly clamped Euler-Bernoulli beams. Because t^* is most often used in typical experimental settings and resulted in better estimates of the torsional stiffness (closer to the LDV method), t^* was used when calculating Eq. (A1) in this paper.

Specifically for the cantilevers calibrated in this paper, the length up to the tip L_{tip} was used for L in both Eqs. (A1) and (A2), instead of the full length L_{full}, because the material past

TABLE III. Parameters describing the PPP-CONTR and PPP-FM cantilevers and their environment.

Parameter	Units	PPP-CONTR		PPP-FM	
		Optical	SEM	Optical	SEM
L_{full}	μm	464.8 ± 1	465.2 ± 1	230.1 ± 1	232.4 ± 1
L_{tip}	μm	446.7 ± 1	445.2 ± 1	224.0 ± 1	226.2 ± 1
L_{spot}	μm	431.9 ± 1	N/A	210.9 ± 1	N/A
w	μm	51.6 ± 1	52.8 ± 1	32.8 ± 1	33.8 ± 1
h_{tip}	μm	14.9 ± 1	15.4 ± 0.1	15.3 ± 1	14.4 ± 0.1
t	μm	N/A	2.0 ± 0.1	N/A	3.1 ± 0.1
t^*	μm	2.154		2.966	
f_N	kHz	14.93		81.76	
f	kHz	251.77		1159.66	
Q		248 ± 5		546 ± 10	
E	GPa	170			
G	GPa	68			
ρ_C	kg/m^3	2328			
ρ	kg/m^3	1.18			
η	μPa s	18.6			

the tip does not contribute to the static torsional stiffness at the tip.

2. Sader method

The Sader method assumes that the hydrodynamic flow around the cantilever can be described as laminar and moving in-plane perpendicular to the long axis of the cantilever by an incompressible fluid. The torsional stiffness can then be calculated by

$$k_{\theta_{DC}} = 0.1592 \rho w^4 L Q \omega^2 \Gamma_i(\omega|\eta, \ \rho, \ w), \qquad (A3)$$

where ρ is the air density and $\Gamma(\omega|\eta, \ \rho, \ w)$ is the hydrodynamic function that is defined elsewhere[44] and is also a function of the air viscosity η.

Specifically for the cantilevers calibrated in this paper, the length up to the tip L_{tip} was used for L, instead of the full length L_{full}, because the mass and hydrodynamic loading become negligible as the cantilever apex tapers off beyond the tip.

3. Calibration parameters

All the calibration parameters used to calculate the spring constants in Table I are summarized in Table III.

[1] S. Maier, Y. Sang, T. Filleter, M. Grant, R. Bennewitz, E. Gnecco, and E. Meyer, Phys. Rev. B **72**, 245418 (2005).
[2] I. Barel, M. Urbakh, L. Jansen, and A. Schirmeisen, Phys. Rev. B **84**, 115417 (2011).
[3] A. Labuda, F. Hausen, N. N. Gosvami, P. H. Grütter, R. B. Lennox, and R. Bennewitz, Langmuir **27**, 2561 (2011).
[4] C. Loppacher, R. Bennewitz, O. Pfeiffer, M. Guggisberg, M. Bammerlin, S. Schär, V. Barwich, A. Baratoff, E. Meyer, and H.-J. Güntherodt, Phys. Rev. B **62**, 13674 (2000).
[5] Z. Liu, S. M. Zhang, J. R. Yang, J. Z. YangLiu, Y. L. Yang, and Q. S. Zheng, Acta Mech. Sin. **28**, 978 (2012).
[6] A. Labuda, M. Lysy, W. Paul, Y. Miyahara, P. Grütter, R. Bennewitz, and M. Sutton, Phys. Rev. E **86**, 031104 (2012).
[7] Y. Dong, H. Gao, A. Martini, and P. Egberts, Phys. Rev. E **90**, 12125 (2014).
[8] X.-Z. Liu, Z. Ye, Y. Dong, P. Egberts, R. W. Carpick, and A. Martini, Phys. Rev. Lett. **114**, 146102 (2015).
[9] Y. Dong, Q. Li, and A. Martini, J. Vac. Sci. Technol., A **31**, 030801 (2013).
[10] M. Müser, Phys. Rev. B **84**, 125419 (2011).
[11] E. Gnecco, R. Bennewitz, T. Gyalog, C. Loppacher, M. Bammerlin, E. Meyer, and H. Guntherodt, Phys. Rev. Lett. **84**, 1172 (2000).
[12] D. Maugis, J. Colloid Interface Sci. **150**, 243 (1992).
[13] R. W. Carpick, D. F. Ogletree, and M. Salmeron, J. Colloid Interface Sci. **211**, 395 (1999).
[14] E. Liu, B. Blanpain, and J. P. Celis, Wear **192**, 141 (1996).
[15] R. G. Cain, M. G. Reitsma, S. Biggs, and N. W. Page, Rev. Sci. Instrum. **72**, 3304 (2001).
[16] J. E. Sader and C. P. Green, Rev. Sci. Instrum. **75**, 878 (2004).
[17] M. A. Lantz, S. J. O'Shea, A. C. F. Hoole, and M. E. Welland, Appl. Phys. Lett. **70**, 970 (1997).
[18] R. W. Carpick, D. F. Ogletree, and M. Salmeron, Appl. Phys. Lett. **70**, 1548 (1997).
[19] D. B. Asay and S. H. Kim, Rev. Sci. Instrum. **77**, 043903 (2006).
[20] R. J. Cannara, M. Eglin, and R. W. Carpick, Rev. Sci. Instrum. **77**, 053701 (2006).
[21] Q. Li, K.-S. Kim, and A. Rydberg, Rev. Sci. Instrum. **77**, 065105 (2006).
[22] E. Tocha, H. Schönherr, and G. J. Vancso, Langmuir **22**, 2340 (2006).
[23] M. Munz, J. Phys. D: Appl. Phys. **43**, 063001 (2010).
[24] N. Mullin and J. K. Hobbs, Rev. Sci. Instrum. **77**, 113703 (2014).
[25] J. E. Sader, Rev. Sci. Instrum. **74**, 2438 (2003).
[26] N. A. Burnham, X. Chen, C. S. Hodges, G. A. Matei, E. J. Thoreson, C. J. Roberts, M. C. Davies, and S. J. B. Tendler, Nanotechnology **14**, 1 (2003).
[27] C. P. Green, H. Lioe, J. P. Cleveland, R. Proksch, P. Mulvaney, and J. E. Sader, Rev. Sci. Instrum. **75**, 1988 (2004).
[28] D. F. Ogletree, R. W. Carpick, and M. Salmeron, Rev. Sci. Instrum. **67**, 3298 (1996).
[29] A. Labuda, J. Cleveland, N. Geisse, M. Kocun, B. Ohler, R. Proksch, M. Viani, and D. Walters, Microsc. Anal. **28**, 23 (2014).
[30] A. Labuda and R. Proksch, Appl. Phys. Lett. **106**, 253103 (2015).
[31] J. E. Sader, J. A. Sanelli, B. D. Adamson, J. P. Monty, X. Wei, S. A. Crawford, J. R. Friend, I. Marusic, P. Mulvaney, and E. J. Bieske, Rev. Sci. Instrum. **83**, 103705 (2012).
[32] A. Labuda, M. Kocun, M. Lysy, T. Walsh, J. Meinhold, T. Proksch, W. Meinhold, C. Anderson, and R. Proksch, Rev. Sci. Instrum. **87**, 073705 (2016).
[33] A. Labuda, Rev. Sci. Instrum. **87**, 033704 (2016).
[34] R. Gates, W. Osborn, and G. Shaw, Nanotechnology **26**, 235704 (2015).
[35] R. S. Gates, W. A. Osborn, and J. R. Pratt, Nanotechnology **24**, 255706 (2013).
[36] W. C. Young and R. G. Budynas, *Roark's Formulas for Stress and Strain*, 7th ed. (McGraw-Hill, New York, 1975).
[37] M. J. Higgins, R. Proksch, J. E. Sader, M. Polcik, S. Mc Endoo, J. P. Cleveland, and S. P. Jarvis, Rev. Sci. Instrum. **77**, 013701 (2006).
[38] K. Wagner, P. Cheng, and D. Vezenov, Langmuir **27**, 4635 (2011).
[39] A. Labuda, W. Paul, B. Pietrobon, R. B. Lennox, P. H. Gruätter, and R. Bennewitz, Rev. Sci. Instrum. **81**, 083701 (2010).
[40] A. Yurtsever, A. M. Gigler, E. Macias, and R. W. Stark, Appl. Phys. Lett. **91**, 253120 (2007).
[41] R. Meyer, E. Hug, and H. Bennewitz, *Scanning Probe Microscopy: The Lab on a Tip* (Springer, 2004), Vol. 45.
[42] A. Khan, J. Philip, and P. Hess, J. Appl. Phys. **95**, 1667 (2004).
[43] M. J. Lachut and J. E. Sader, Phys. Rev. Lett. **99**, 206102 (2007).
[44] J. E. Sader, J. Appl. Phys. **84**, 64 (1998).
[45] A. Labuda and P. H. Grütter, Rev. Sci. Instrum. **82**, 013704 (2011).
[46] J. Tamayo, V. Pini, P. Kosaka, N. F. Martinez, O. Ahumada, and M. Calleja, Nanotechnology **23**, 315501 (2012).
[47] R. Proksch, J. Appl. Phys. **118**, 072011 (2015).
[48] H. Chen and T. Filleter, Nanotechnology **26**, 135702 (2015).
[49] M. Daly, C. Cao, H. Sun, Y. Sun, T. Filleter, and C. V. Singh, ACS Nano **10**, 1939 (2016).
[50] This equation was derived by equating the strain energy integrals of both mode shapes to the respective stiffnesses by the equipartition theorem and then taking the ratio of both equations. Combining both equations into a single one is valid because both mode shapes share the same coordinate system.
[51] At small amplitudes, the digital-to-analog digitization of the cantilever deflection signal by the Polytec LDV causes a bias in the estimation of the overall thermal fluctuations measured by the Cypher AFM electronics.